Non-Markovian reduced dynamics of ultrafast charge transfer at an oligothiophene–fullerene heterojunction

Hughes, K.H.; Cahier, B.; Martinazzo, R.; Tamura, H.; Burghardt, I.

Chemical Physics

DOI:
10.1016/j.chemphys.2014.06.015

Published: 09/07/2014

Peer reviewed version

Non-Markovian reduced dynamics of ultrafast charge transfer at an oligothiophene-fullerene heterojunction

Keith H. Hughes[a,*], Benjamin Cahier[a], Rocco Martinazzo[b], Hiroyuki Tamura[c], Irene Burghardt[d]

[a] *School of Chemistry, Bangor University, Bangor, Gwynedd LL57 2UW, UK.*
[b] *Dipartimento di Chimica-Fisica ed Elettrochimica, Università degli Studi di Milano, v. Golgi 19, 20133 Milano, Italy.*
[c] *WPI-Advanced Institute for Material Research, Tohoku University, 2-1-1 Katahira, Aoba-ku, Sendai, 980-8577, Japan.*
[d] *Institute of Physical and Theoretical Chemistry, Goethe University Frankfurt, Max-von-Laue-Str. 7, 60438, Frankfurt/Main, Germany.*

Abstract

We extend our recent quantum dynamical study of the exciton dissociation and charge transfer at an oligothiophene-fullerene heterojunction interface (H. Tamura, R. Martinazzo, M. Ruckenbauer, and I. Burghardt, J. Chem. Phys. 137 (2012) 22A540) by investigating the process using the non-perturbative hierarchical equations of motion (HEOM) approach. Based upon an effective mode reconstruction of the spectral density the effect of temperature on the charge transfer is studied using reduced density matrices. It was found that the temperature had little effect on the charge transfer and a coherent dynamics persists over the first few tens of femtoseconds, indicating that the primary charge transfer step proceeds by an activationless pathway.

Keywords: Organic photovoltaics, non-Markovian, HEOM, spectral density, exciton dynamics

1. Introduction

The key processes involved in charge and energy transfer in organic photovoltaics occur over various timescales. Upon generation of a Frenkel exciton (the XT state) following absorption of light in the organic photovoltaic material the exciton diffuses to the organic heterojunction interface to form a localised charge transfer (CT) state [1, 2]. The diffusion lengths are typically 10-20 nm and the timescale for the exciton diffusion is typically 1 ps to 1 ns. In so-called bulk heterojunction (BHJ) architectures [3], a significant portion of excitons are generated at or close to the heterojunction interface, and the exciton generation and dissociation is then an ultrafast femtosecond process - this is the scenario addressed in

*Corresponding author
Email address: keith.hughes@bangor.ac.uk (Keith H. Hughes)

this work. At the interface the CT state is formed on an ultrafast timescale of around 50 - 200 fs. The CT state is then delocalised as the electron is transferred into the material with highest electron affinity (acceptor) and the hole is transferred to the material with lowest ionisation potential (donor). The electron and hole can then transfer to the electrodes over a nanosecond to microsecond timescale. The charge and energy transfer is strongly influenced by electron-phonon coupling [2, 4, 5, 6].

Currently, the best performing polymer solar cells use donor/acceptor blends with thiophene based donor polymers and fullerene acceptor species. Power conversion efficiencies of up to 10% were very recently achieved with PTB7:$PC_{70}BM$ junctions [9], while the paradigm heterojunction material P3HT:PCBM (poly(3-hexylthiophene): [6,6]-phenyl-C_{61}-butyric acid methyl ester) yields approximately 5%. Although this percentage is relatively low in comparison to inorganic solar cells, which have a power conversion efficiency of around 22%, organic photovoltaics have the advantage of low production costs and physical flexibility of the material, as well as superior low-light and high-temperature performance.

Following Refs. [5, 6], the oligothiophene OT_4 (donor) and fullerene C_{60} complex depicted in Fig. 1 is used in this work as a model to describe a fragment of the P3HT:PCBM interface. The model is relevant to describe the P3HT:PCBM heterojunction because the alkyl chains of the P3HT have a very low impact on the π molecular orbitals which are relevant to describe the exciton dissociation. A key difference between OT_4 and P3HT is that the longer π conjugation length for P3HT lowers the exciton energy. For C_{60} and PCBM an important difference in their electronic structure is that the LUMO of C_{60} is triply degenerate but the degeneracy is broken in PCBM due to symmetry loss [10]. However, these differences have a very low impact on the charge transfer efficiency. Other key aspects, like the aggregation of P3HT and PCBM in regioregular structures [11] that strongly influences the nature of the primary excitations and the CT state, are disregarded in the present work (see, however, Ref. [12] for a more complete treatment).

The key focus of this work is the study of the dynamics of the XT to CT transfer in the OT_4:C_{60} complex that occurs on the femtosecond timescale. For this system the diabatic coupling is comparatively strong [5] and the charge transfer dynamics is ultrafast such that the XT population dynamics cannot be approximated by Marcus theory and requires a more explicit treatment of the dynamics. In Refs. [5, 6] the XT population dynamics were computed explicitly by numerical solution of the time-dependent Schrödinger equation using the multiconfiguration time-dependent Hartree (MCTDH) method [14, 15, 16] (Heidelberg MCTDH package [17]). Their simulations involved sampling a discrete set of frequencies for the OT_4 and C_{60} modes that were taken in their ground vibrational states which related to a temperature $T = 0$ K simulation for the bath.

In the oligothiophene-fullerene complex the reorganisation energy λ is quite small and the XT$\rightarrow$CT transfer is a nearly activationless process occurring in the Marcus inverted region, and is expected to be temperature independent. Furthermore, the experimental observations of Asbury *et al.* [7, 8, 4] indicate that the process is temperature independent. However, one might expect that the ensuing charge separation could show some temperature dependence due to the Coulomb barrier to electron-hole separation. Experimentally, several experimental studies point to negligible temperature effects [7, 19] while

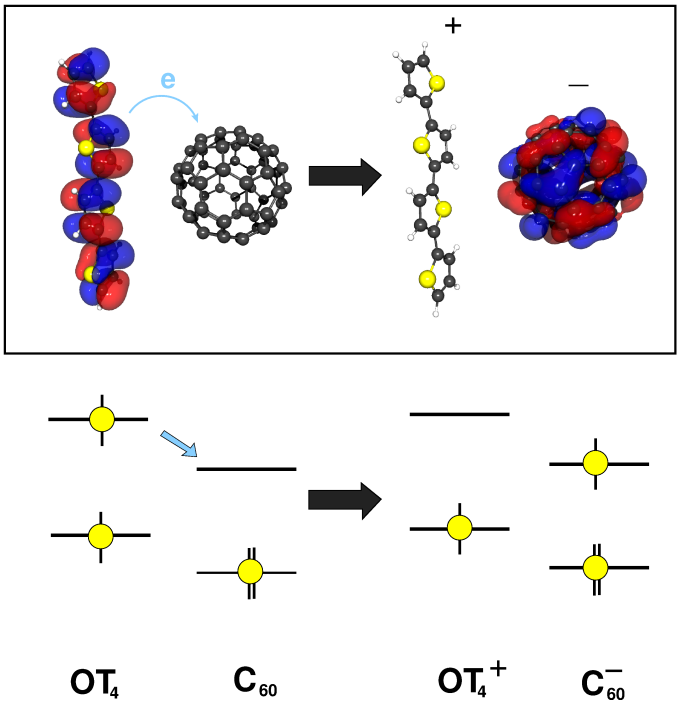

Figure 1: Structural (top) and energetic (bottom) representation of the oligothiophene OT_4 fullerene C_{60} complex in the XT state on the left, and the OT_4^+:C_{60}^+ complex in the CT state on the right. The LUMO orbitals of the OT_4 and C_{60} moieties are also illustrated.

some investigations have provided evidence for a temperature dependence in experimentally observed photocurrents [18]. Recent experiments and quantum dynamical simulations suggest that a combination of charge delocalisation and vibronic excess energy entail an ultrafast, temperature independent formation of charge separated states [12, 13].

To investigate any temperature dependency of the primary exciton dissociation step, the XT population dynamics in this work are computed explicitly using reduced density matrix methods which allows simulations to be made at different temperatures. The approach adopted is the non-perturbative hierarchical equations of motion approach [20, 21, 22, 23] (HEOM). In a reduced density matrix approach the Hamiltonian is partitioned into a system and bath part, and a coupling between the system-bath which is characterised by the spectral density $J_0(\omega)$. The spectral density can be obtained experimentally [24], by molecular dynamics simulation, or from geometry-dependent electronic structure calculations, as is the case in the present work [5]. Phenomenological spectral densities such as the Ohmic form $J_0(\omega) = \eta\omega$ are widely used due to their simple form. However, the spectral density is often highly structured and cannot be represented by a simple phenomenological form. Complicated and highly structured spectral densities are prevalent in many biological processes and play an important role in the dynamics of such processes [25].

In Refs. [26, 27, 28, 29, 30] it was shown that an effective mode representation of the spectral density captures the essential features of highly structured spectral densities. The effective spectral densities are based on the construction of effective modes of the

environment. The resulting effective spectral density takes the form of the imaginary part of a continued fraction but the corresponding bath correlation function is a series of exponential terms which is conveniently in the correct form required for the HEOM. We recently explored the use of effective-mode correlation functions in a second-order non-Markovian setting [36] using time local (TL) and time non-local (TNL) master equations. The present work extends this study to a systematic non-perturbative treatment.

The remainder of the paper is organised as follows. We first describe the Hamiltonian for the oligothiophene-fullerene heterojunction (Sec. 2) and then formulate the construction of the effective mode representation of the spectral density and bath correlation function in Sec. 3. Sec. 4 summarises the HEOM approach. Results are presented in Sec. 5, and finally, Sec. 6 concludes.

2. Oligothiophene-Fullerene Heterojunction Hamiltonian

The total Hamiltonian of the XT to CT transfer in the OT_4:C_{60} complex is given by [6]

$$\hat{H} = \hat{H}_S + \hat{H}_{SB} + \hat{H}_B \tag{1}$$

which consists of a two-level system coupled to a bath of harmonic oscillators,

$$\hat{H}_B = \sum_j \frac{1}{2}(\hat{p}_j^2 + \omega_j^2 \hat{x}_j^2) \tag{2}$$

where $\hat{p}_j$ and $\hat{x}_j$ are the momenta and position of the jth bath harmonic oscillator with frequency ω_j and mass-weighted coordinates are used throughout. The two-level system part consists of the charge transfer state and the exciton state, and is given by

$$\hat{H}_S = -\Delta_{\mathrm{XT-CT}}|\mathrm{CT}\rangle\langle\mathrm{CT}| + \gamma(|\mathrm{XT}\rangle\langle\mathrm{CT}| + |\mathrm{CT}\rangle\langle\mathrm{XT}|) \tag{3}$$

where $\Delta_{\mathrm{XT-CT}} = 0.00290$ a.u. is the XT to CT electronic energy gap and the diabatic coupling $\gamma = 0.00478$ a.u. was evaluated at a distance of 3.0 Å between the donor and acceptor. In Refs. [5, 6], a dependency of the coupling on the inter-fragment distance was taken into account that is neglected in the present treatment.

The system-bath coupling is given by

$$\hat{H}_{SB} = |\mathrm{CT}\rangle\langle\mathrm{CT}| \sum_j c_j \hat{x}_j \tag{4}$$

where the coupling coefficients c_j are related to the spectral density

$$J_0(\omega) = \frac{\pi}{2} \sum_j \frac{c_j^2}{\omega_j} \delta(\omega - \omega_j) \tag{5}$$

In this work the spectral density is constructed from a continuous representation of a discrete, normal-mode based distribution of the electron-phonon couplings, as described in Ref. [6]. In addition, the OT_4:C_{60} inter-fragment coordinate is incorporated into the bath spectral density, while in Ref. [6] this coordinate was treated explicitly as part of the quantum subsystem.

Briefly, the procedure for obtaining a continuous form of the spectral density involved generating a Lorentzian broadening of $N_0 = 265$ discrete points (from the normal modes plus inter-fragment coordinate) as follows,

$$\begin{aligned} J_0(\omega) &= \frac{\pi}{2}\sum_{j=1}^{N_0}\frac{c_j^2}{\omega_j}\delta(\omega-\omega_j) \\ &\simeq \frac{\pi}{2}\sum_{j=1}^{N_0}\frac{c_j^2}{\pi\omega_j}\frac{\Delta\omega}{(\omega-\omega_j)^2+(\Delta\omega)^2} \end{aligned} \tag{6}$$

where Δ is the the root-mean-square of the frequency spacing of the discrete distribution of the electron-phonon couplings.

The continuous form of the spectral density yields a more realistic representation of a dissipative environment. As detailed in the next section, this continuous spectral density will be subsequently used to map the dissipative system into a complementary Hamiltonian representation that is particularly suited to obtain a reduced-dimensional non-Markovian dynamics. This representation is related to an effective-mode description of the bath [26, 27, 28, 29, 30, 31, 32, 33, 34], as further detailed below.

3. Effective Mode Representation and Rational Approximants to the Spectral Density

The spectral density $J_0(\omega)$ as obtained above is generally highly structured, such that approximations are necessary. Among various possible approximation schemes, we focus in the following on a rational approximation of the spectral density (Sec. 3.2) which naturally leads to open-system, non-Markovian models that can be solved with the Hierarchical Equation of Motion (HEOM) approach (Sec. 4). The rational approximation is derived from an effective mode construction (Sec. 3.1) of the system-bath Hamiltonian that yields a Hamiltonian model with an infinite but countable bath degrees of freedom. Such an effective mode representation naturally leads to controlled approximations to the bath response at short times, which can be made exact for increasingly longer time-scales by increasing the number of modes introduced.

3.1. Effective-mode transformation and residual spectral densities

The abovementioned effective mode transformation of the system-bath Hamiltonian involves a coordinate transformation of the Hamiltonian that leaves the system part unaffected. The first step of the transformation is to subsume the complete system-bath

interaction into a single effective mode $\hat{X}_1$ [26, 28, 34] (see also earlier works [39, 41]),

$$\hat{H}_{SB} = |\mathrm{CT}\rangle\langle\mathrm{CT}| \sum_j c_j \hat{x}_j = |\mathrm{CT}\rangle\langle\mathrm{CT}| D_{0,1} \hat{X}_1 \tag{7}$$

where

$$\hat{X}_1 = \frac{\sum_j c_j \hat{x}_j}{D_{0,1}} = \frac{\sum_j c_j \hat{x}_j}{(\sum_j c_j^2)^{1/2}} \tag{8}$$

In this form the short-time dynamics is accounted for entirely by the system and effective mode only. For longer time-scales the residual bath modes need to be included in the dynamics. The residual bath modes $\hat{X}_2 \ldots \hat{X}_{N_B}$ can be constructed in a number of ways provided they are orthogonal [26, 33, 35].

If the initial spectral density $J_0(\omega)$ of Eq. (6) is a smooth, continuous function representing a truly dissipative system, the coupling $D_{0,1}$ and the effective mode frequency Ω_1 are extracted from $J_0(\omega)$ in terms of frequency moments of $J_0(\omega)$ [29],

$$D_{0,1}^2 = \frac{2}{\pi} \int_0^\infty \omega J_0(\omega) d\omega \tag{9}$$

$$\Omega_1^2 = \frac{2}{D_{0,1}^2 \pi} \int_0^\infty \omega^3 J_0(\omega) d\omega \tag{10}$$

This procedure implicitly defines a *residual spectral density* $J_1(\omega)$ describing the coupling of the X_1 mode to the residual bath [29, 30]. For $J_1(\omega)$, the above construction scheme can be reiterated such as to extract a second effective mode X_2 that is in turn coupled to a residual spectral density $J_2(\omega)$. In general, the $n+1$-th effective mode frequency Ω_{n+1} and coupling $D_{n,n+1}$ are evaluated as in Eqs. (9) and (10) using the *n-th* residual spectral density $J_n(\omega)$ characterizing the bath.

This provides a general recipe for computing the effective mode parameters entering in the resulting semi-infinite linear chain representation of the bath,

$$\hat{H}_B = \sum_{n=1}^{\infty} \frac{1}{2} (\hat{P}_n^2 + \Omega_n^2 \hat{X}_n^2) + \sum_{n=1}^{\infty} D_{n,n+1} \hat{X}_n \hat{X}_{n+1}. \tag{11}$$

An alternative route to obtaining the tridiagonal form Eq. (11) involves an orthogonal coordinate transformation [26, 27, 31, 32, 33, 35]. In the limit of an infinite number of bath modes, the combination of Eq. (7) and Eq. (11) for $H_{SB} + H_B$ is strictly equivalent to the original form of the Hamiltonian of Eq. (2) and Eq. (4). The tridiagonal chain form of Eq. (11) has been referred to as hierarchical electron-phonon (HEP) model [31, 32].

The *n-th* residual spectral density $J_n(\omega)$ is the limiting imaginary part of a generating (propagator) function $W_n(z)$ [29],

$$J_n(\omega) = \mathrm{Im} \lim_{\epsilon \to 0^+} W_n(\omega + i\epsilon) \tag{12}$$

which satisfies a simple recursion [29]

$$W_n(z) = \Omega_n^2 - z^2 - \frac{D_{n-1,n}^2}{W_{n-1}(z)} \tag{13}$$

to be started with

$$W_0(z) = \frac{1}{\pi}\int_{-\infty}^{+\infty} \frac{J_0(\omega)}{z-\omega} d\omega$$

It was shown [29] that, under quite general conditions, the recurrence converges to a quasi-Ohmic (Rubin [37]) spectral density.

3.2. Rational approximants of the spectral density

In view of the above, the original spectral density $J_0(\omega)$ can be re-written to make explicit its dependence on the first M effective mode parameters, namely [26, 29, 39]

$$J_0(\omega) = \mathrm{Im} \lim_{\epsilon \to 0^+} W_0(\omega + i\epsilon) \tag{14}$$

with the continued-fraction form [26, 29]

$$W_0(z) = \cfrac{D_{0,1}^2}{\Omega_1^2 - z^2 - \cfrac{D_{1,2}^2}{\Omega_2^2 - z^2 - \cdots \cfrac{D_{M-1,M}^2}{\Omega_M^2 - z^2 - W_M(z)}}}$$

as follows readily upon solving the recurrence in Eq.(13) for $W_{n-1}(z)$ in terms of $W_n(z)$.

Thus, replacing $W_M(z)$ with an effective closing function $I(z)$ one obtains an Mth order approximant that makes use of the first M effective mode parameters [26, 27]. Of particular interest, in conjuction with the HEOM approach to be discussed below, is the Markovian (Ohmic) closure $I(z) = i\eta z$ (where η is a friction coefficient) which generates an $M-th$ order *rational* approximant of the spectral density, that is $J_{\mathrm{eff}}^{(M)}(\omega) = \mathrm{Im}\lim_{\epsilon\to 0^+} W_{\mathrm{eff}}^{(M)}(\omega + i\epsilon)$ where

$$W_{\mathrm{eff}}^{(M)}(z) = \cfrac{D_{0,1}^2}{\Omega_1^2 - z^2 - \cfrac{D_{1,2}^2}{\Omega_2^2 - z^2 - \cdots \cfrac{D_{M-1,M}^2}{\Omega^2{}_M - z^2 + i\eta z}}} \text{The}$$

resulting $M-th$ order effective spectral density can also be written as

$$J_{\mathrm{eff}}^{(M)}(\omega) \;\; = \;\; \eta\omega \frac{\Pi_{n=1}^M D_{n-1,n}^2}{A^{(M)}(\omega) A^{(M)*}(\omega)} \tag{15}$$

where $A^{(M)}(\omega)$ is a polynomial of order $2M$ in the frequency ω which follows from the recursion

$$\begin{aligned} A^{(1)}(\omega) &= \Omega_M^2 - \omega^2 + i\eta\omega \\ A^{(2)}(\omega) &= (\Omega_{M-1}^2 - \omega^2)A^{(1)}(\omega) - D_{M-1,M}^2 \\ A^{(3)}(\omega) &= (\Omega_{M-2}^2 - \omega^2)A^{(2)}(\omega) - D_{M-2,M-1}^2 A^{(1)}(\omega) \\ \cdots \quad & \quad \cdots \quad \cdots \quad \cdots \\ A^{(M)}(\omega) &= (\Omega_1^2 - \omega^2)A^{(M-1)}(\omega) - D_{1,2}^2 A^{(M-2)}(\omega) \end{aligned} \tag{16}$$

Such Mth order approximations progressively capture the details of realistic, highly structured spectral densites and thus describe bath memory effects on increasingly longer time scales. More precisely, when the closure is implemented at the Mth level the memory kernel is reproduced correctly up to the $(4M+1)$th order in time [30].

3.3. Bath Correlation Function

The second-order bath correlation function $C_B(t)$,

$$C_B(t) = D_{0,1}^2 \mathrm{Tr}\Big\{ \hat{X}_1(0)\hat{X}_1(t)\hat{\rho}_B^{\mathrm{eq}} \Big\} \tag{17}$$

is related to the spectral density as follows [36, 38, 39, 40],

$$C_B(t) = \frac{1}{\pi}\int_0^\infty d\omega J_0(\omega)[\coth(\beta\omega/2)\cos(\omega t) - i\sin(\omega t)] \tag{18}$$

where $\beta = (k_B T)^{-1}$, k_B is Boltzmann's constant and T is the temperature of the bath. The integral of Eq. (18) is usually solved by contour integration after substituting the expansion of the hyperbolic cotangent function in terms of Matsubara frequencies $\nu_l = 2\pi l/\beta$

$$\coth(\beta\omega/2) = \frac{2}{\beta}\Big(\frac{1}{\omega} + 2\sum_{l=1}^{l=\infty}\frac{\omega}{\omega^2+\nu_l^2}\Big) \tag{19}$$

The summation in Eq. (19) is only infinite for $T = 0$ K but converges at some finite value n_{mat} for non-zero temperatures.

The approximate bath correlation function obtained from Eq. (18) using the Mth-order effective spectral density defined in Eq. (15) is given by [36]

$$C_B^{(M)}(t) = \sum_{l=1}^{n_{\mathrm{exp}}} g_l \exp(h_l t) - i\sum_{l=1}^{2M} f_l \exp(h_l t) \tag{20}$$

where $n_{\mathrm{exp}} = 2M + n_{\mathrm{mat}}$ is the total number of exponential terms in $C_B^{(M)}(t)$ - there are n_{mat} terms arising from the poles of the Matsubara summation and $2M$ terms arising from

the effective modes. In Eq. (20) h_l are the poles in the lower part of the complex plane for $z = \omega + i\epsilon$

$$\begin{aligned} h_l &= -ip_l \quad l \leq 2M \\ &= -\nu_l \quad l > 2M \end{aligned} \tag{21}$$

The poles p_l can be found by solving $A^{(M)}(z) = 0$. The coefficients in Eq. (20) are given by,

$$f_l = \eta \Pi_{n=1}^{M} D_{n-1,n}^2 \frac{p_l}{\Pi_{i \neq l}(p_i - p_l)}, \tag{22}$$

and for $l \leq 2M$

$$g_l = -i\eta \Pi_{n=1}^{M} D_{n-1,n}^2 \frac{p_l}{\Pi_{i \neq l}(p_i - p_l)} \coth\left(\frac{\beta}{2} p_l\right), \tag{23}$$

otherwise

$$g_l = -\frac{2}{\beta} \eta \Pi_{n=1}^{M} D_{n-1,n}^2 \frac{\nu_l}{B_n^{(M)} B_n^{(M)\dagger}}, \tag{24}$$

where $B_n^{(k)}$ is a real function with the following recursion

$$\begin{aligned} B_n^{(1)} &= \Omega_M^2 + \nu_n^2 + \eta\nu_n \\ B_n^{(2)} &= (\Omega_{M-1}^2 + \nu_n^2) B_n^{(1)} - D_{M-1,M}^2 \\ B_n^{(3)} &= (\Omega_{M-2}^2 + \nu_n^2) B_n^{(2)} - D_{M-2,M-1}^2 B_n^{(1)} \\ \cdots &\quad \cdots \quad \cdots \quad \cdots \\ B_n^{(M)} &= (\Omega_1^2 + \nu_n^2) B_n^{(M-1)} - D_{1,2}^2 B_n^{(M-2)} \end{aligned} \tag{25}$$

and

$$\begin{aligned} B_n^{(1)\dagger} &= \Omega_M^2 + \nu_n^2 - \eta\nu_n \\ B_n^{(2)\dagger} &= (\Omega_{M-1}^2 + \nu_n^2) B_n^{(1)\dagger} - D_{M-1,M}^2 \\ B_n^{(3)\dagger} &= (\Omega_{M-2}^2 + \nu_n^2) B_n^{(2)\dagger} - D_{M-2,M-1}^2 B_n^{(1)\dagger} \\ \cdots &\quad \cdots \quad \cdots \quad \cdots \\ B_n^{(M)\dagger} &= (\Omega_1^2 + \nu_n^2) B_n^{(M-1)\dagger} - D_{1,2}^2 B_n^{(M-2)\dagger} \end{aligned} \tag{26}$$

Once the poles have been determined, the correlation function $C_B^{(M)}$ can be constructed from Eq. (20). This generalizes the procedure of Ref. [36] where analytical expressions were obtained for some low-order effective-mode correlation functions.

4. Quantum Dynamical Equations

To study the dynamics of the exciton dissociation the hierarchical equations of motion (HEOM) approach [20, 21, 22, 23, 41] is used in conjunction with M-th order effective-mode correlation functions as defined above. The HEOM, which can be derived from a path integral representation [20, 21, 22] or from the stochastic Liouville equation approach [23, 41], is a non-perturbative approach to system-bath quantum dynamics and can be used for systems that are strongly coupled to a thermal bath. The HEOM approach has been applied to processes such as proton transfer [42, 43], electron transfer [44, 45, 46, 47] and excitation energy transfer in light harvesting complexes [48, 49, 50, 51].

As the name suggests the HEOM involve a hierarchy of equations for auxiliary density operators (ADOs) associated with different levels of the hierarchy, where each level displays coupling to the next higher and lower levels of the hierarchy. The HEOM can be expressed as

$$\begin{aligned}\frac{\partial\hat{\rho}_{\mathbf{n}}}{\partial t} &= (-i\hat{\hat{\mathcal{L}}}_S + \sum_{k=1}^{n_{\rm exp}} n_k h_k)\hat{\rho}_{\mathbf{n}} - i\sum_{k=1}^{n_{\rm exp}}[\hat{H}_{\rm op}, \hat{\rho}_{\mathbf{n}^+}] \\ &\quad -i\sum_{k=1}^{n_{\rm exp}} g_k n_k[\hat{H}_{\rm op}, \hat{\rho}_{\mathbf{n}^-}] - \sum_{k=1}^{2M} f_k n_k[\hat{H}_{\rm op}, \hat{\rho}_{\mathbf{n}^-}]_+ \end{aligned} \tag{27}$$

where $\hat{H}_{\rm op} = |{\rm CT}\rangle\langle{\rm CT}|$ represents the system component of $\hat{H}_{SB}$ and $\hat{\hat{\mathcal{L}}}_S = [\hat{H}_S, \bullet]$. The influence of the bath is manifest in the bath correlation function coefficients f_k, g_k, h_k as defined in Eq. (20). For a given hierarchy level n the term $\mathbf{n}$ is shorthand notation for the $n_{\rm exp}$ digit non-negative integer index of the ADOs, where each index labels an exponential term in the summation of Eq. (20). For example, if $n_{\rm exp} = 3$ there are $n_{\rm exp}$ ADOs at the $n = 1$ hierarchy level labelled $\hat{\rho}_{100}$, $\hat{\rho}_{010}$ and $\hat{\rho}_{001}$. At $\mathbf{n} = 0$, $\rho_{\mathbf{0}}$ is the reduced system density operator and here is a 2×2 matrix associated with the CT and XT electronic states.

The terms $\mathbf{n}^+$ and $\mathbf{n}^-$ correspond to hierarchy upcoupling to level $\mathbf{n} + \mathbf{1}$ and downcoupling to $\mathbf{n} - \mathbf{1}$ respectively. In terms of the $n_{\rm tot}$ digit index of the ADOs only ADOs that raises (lowers) each of the indices by +1(-1) contribute to the upcoupling (downcoupling). For example, at the $n = 1$ hierarchy level the ADO $\hat{\rho}_{010}$ will upcouple to $\hat{\rho}_{110}, \hat{\rho}_{020}$ and $\hat{\rho}_{011}$ and can downcouple only to $\hat{\rho}_{000}$ which is the reduced system density matrix.

The terms n_k in Eq. (27) are non-negative integers equal to the indeces of the ADO concerned.

The HEOM hierarchy defined in Eq. (27) is infinite and has to be truncated at some level. The number of ADOs associated with a given hierarchy level is given by $(n_{\rm exp} + n)!/[n!(n_{\rm exp} - 1)!]$, where n is the hierarchy level. To be of any numerical use the hierarchy truncation level should not be too high. Commonly used truncation schemes involve a Markovian closure at the highest level n_H, or setting all ADOs to zero for the $n_H + 1$ level - the so called time-nonlocal (TNL) closure. In this work the TNL closure was found to be most stable.

It should be emphasised that the hierarchy associated with the HEOM is distinct from the effective mode hierarchy of Sec. 3. The present scheme therefore involves a *dual* hierarchy of effective modes and HEOM levels.

5. Results and Discussion

The spectral density $J_0(\omega)$ obtained from the electronic structure calculations of Ref. [6], and constructed in continuous from as described in Sec. 2, is depicted in Fig. 2a). For the effective mode deconvolution of $J_0(\omega)$ a frequency cut-off of 5000 cm^{-1} was used in the iterative routine of Secs. 3.1-3.2 and full convergence to quasi-Ohmic form was obtained with 40 effective modes. The spectral density between the nth effective mode and the residual bath, ie $J_n(\omega)$ is depicted in Fig. 2b) for various values of n. Although 40 effective modes are required for full convergence to quasi-Ohmic form this number is too high to be used for generating the correlation function required for the HEOM approach and so the closure to the effective mode chain needs to be implemented at a much lower level. Fig. 2b) illustrates that $J_n(\omega)$ is sufficiently well converged by $n = 5 - 6$.

For the effective mode reconstruction of the spectral density using Eq. (15) the Ohmic friction term η was evaluated from a linear regression of the small frequency part of $J_{M+1}(\omega)$. The resulting reconstructed effective mode spectral density $J^{(M)}_{\rm eff}(\omega)$ for $M = 4, 5$ and 6 is depicted in Fig. 3 alongside $J_0(\omega)$. Although $J^{(M)}_{\rm eff}(\omega)$ does not resemble $J_0(\omega)$ the effective mode spectral densities capture the essential physics of the environment's collective response modes and, as demonstrated extensively in Ref. [30], reproduces the memory kernel up to $4n$th order in time. This is the key strength of the effective mode approach - that the system-bath dynamics is accurately reproduced as the length of the effective mode chain increases, and this is illustrated in Fig. 4 which illustrates the bath correlation functions associated with $J_0(\omega)$ and $J^{(M)}(\omega)$ for $M = 4$, 5 and 6. For the system quantum dynamics the influence of the bath correlation function is most dominant at early times where the initial oscillatory decay of $C_B(t)$ occurs over the first 13 fs. The correlations at longer times are important but not as dominant as early times. It is crucial therefore that $C^{(M)}(t)$ captures the early dynamics accurately. At the $M = 4$ level the first oscillation is not captured. The $M = 5$ and $M = 6$ hierarchy levels captures very closely the first oscillation decay of $C_B^{(M)}(t)$; however, over longer timescales the deviation of $C_B^{(M)}(t)$ from $C_B(t)$ is more pronounced for $C_B^{(6)}(t)$ - $C_B^{(5)}(t)$ is closer to $C_B(t)$ beyond 25 fs. Increasing the effective mode chain length beyond $M = 6$ has a drastic influence on the numerical effort for simulating the system dynamics using the HEOM approach; consequently, the effective mode hierarchy was implemented at the $M = 5$ level. The effective mode parameters for $C_B^{(5)}(t)$ are defined in Table 1 and were constructed using the procedure described in Sec. 3.

The dynamical calculations illustrated here were carried out using the HEOM method described in Sec. 4. The system-bath coupling was strong enough to necessitate a 10th level hierarchy for the HEOM. At this high level the computations become numerically intensive and with an effective mode closure at the $M = 5$ level, which gives rise to 10 exponential terms in $C^{(5)}(t)$, there are $(n_{\rm exp} + n)!/[n!(n_{\rm exp} - 1)!] = 1847560$ ADOs at the

Ω_1	Ω_2	Ω_3	Ω_4	Ω_5	η
0.0077	0.017	0.016	0.016	0.012	0.062
D_{01}	D_{12}	D_{23}	D_{34}	D_{45}	
5.82×10^{-4}	5.45×10^{-4}	1.42×10^{-4}	1.40×10^{-4}	1.32×10^{-4}	

Table 1: Effective mode frequencies Ω_i and coupling parameters D_{ij} in mass weighted coordinates and quoted in atomic units for an effective mode closure at the $M = 5$ level.

$n = 10$ level hierarchy for the HEOM – and this is without consideration of the Matsubara exponential terms.

We re-emphasise here that the hierarchy associated with the HEOM is distinct from the effective mode hierarchy of Sec. 3. The HEOM truncation depends on the strength of the system-bath coupling. For the effective mode hierarchy the coupling between the final effective mode in the chain with the bath may still be large. The effective mode inter-chain couplings do not necessarily become progressively weaker along the chain – the convergence criterion is that the spectral density felt by the final effective mode of the chain becomes quasi-Ohmic. For the HEOM, however, the ADOs do become progressively smaller as the hierarchy level increases, until eventually they become negligible.

Using the effective mode spectral density the HEOM is exceptionally challenging: each effective mode incorporated into the spectral density gives rise to two exponential terms in $C_B^{(M)}(t)$, and for a high level HEOM truncation the number of ADOs becomes large. Consequently, the number of Matsubara frequencies (each frequency contributes one exponential term to $C_B^{(M)}(t)$) were limited to zero or five. At low temperatures the number of Matsubara frequencies required for convergence is large. For low temperatures the Ishizuki-Tanimura truncation [22] is applied to the Matsubara frequencies of the expansion of Eq. (20). The Ishizuki-Tanimura truncation applies the Markov approximation $\nu_l \exp(-\nu_l t) \simeq \delta(t)$ for Matsubara frequencies where $l > n_{\rm mat}$, which results in inclusion of the term

$$\hat{\dot{\mathcal{L}}}_{\rm Markov} = -\sum_{l=n_{\rm exp}+1}^{\infty} g_l[\hat{H}_{\rm op}, [\hat{H}_{\rm op}, \hat{\rho}_{\mathbf{n}}]] \tag{28}$$

in Eq. (27).

As an initial condition the XT state was initially populated for the system density matrix $\hat{\rho}_{\mathbf{0}}^{\rm XT,XT}(t=0) = 1$ and all ADOs set to zero $\hat{\rho}_{\mathbf{n}>\mathbf{0}}(t=0) = 0$. The HEOM was propagated using a 4th order Runge-Kutta time integrator for time steps of $\Delta t = 1$ a.u..

The key result illustrated here is the exciton population and coherence decay at different temperatures. In Ref. [6] it was shown that the exciton population decayed rapidly down to a population of 0.3 in less than 10 fs and then slowly equilibrated in an oscillatory manner over 100 fs to a population of around 0.2. As detailed in Ref. [6] the initial exciton population decay is mediated by the electronic coherence which then dephases due to the coupling to the vibrations. However, the dynamics of Ref. [6] were computed using the MCTDH wavepacket approach which relates to a $T = 0$ K simulation for the bath. In

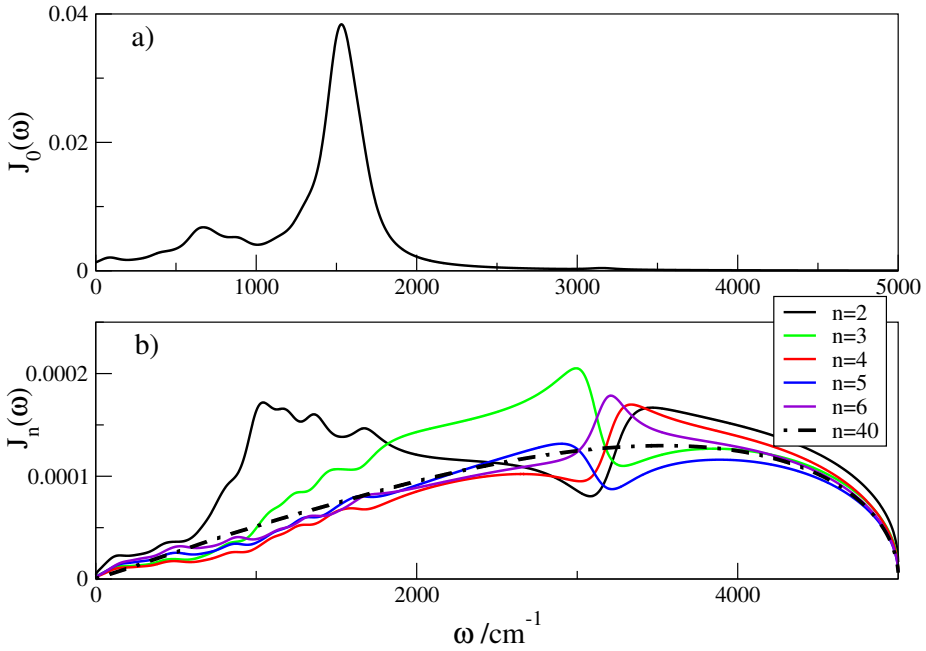

Figure 2: a) Spectral density $J_0(\omega)$ and b) residual spectral densities $J_n(\omega)$ for $n = 2 - 6$ and $n = 40$.

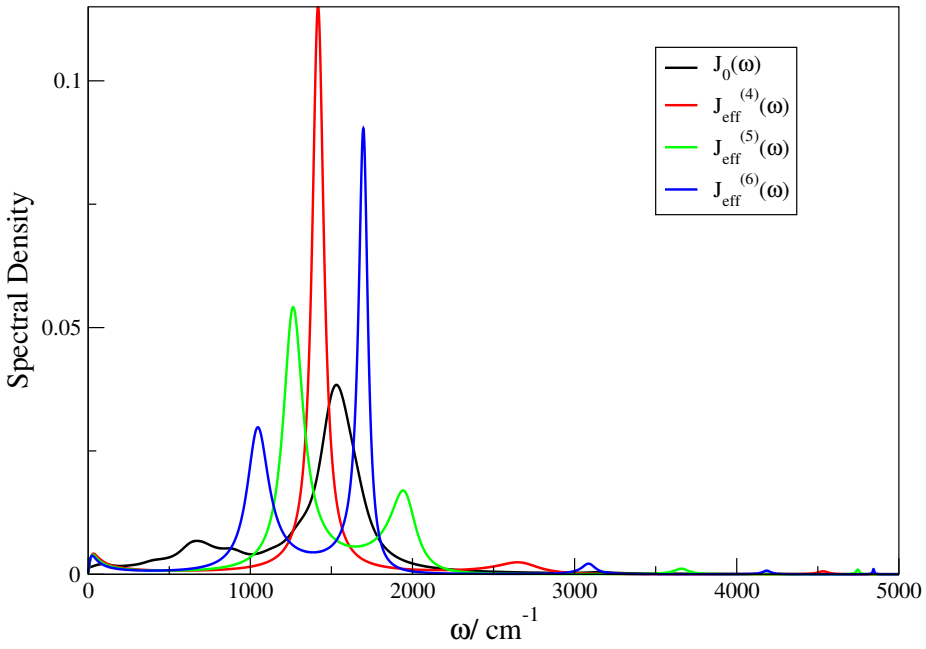

Figure 3: Spectral density $J_0(\omega)$ and effective mode reconstructed spectral densities $J_{\rm eff}^{(M)}(\omega)$ for $M = 4-6$.

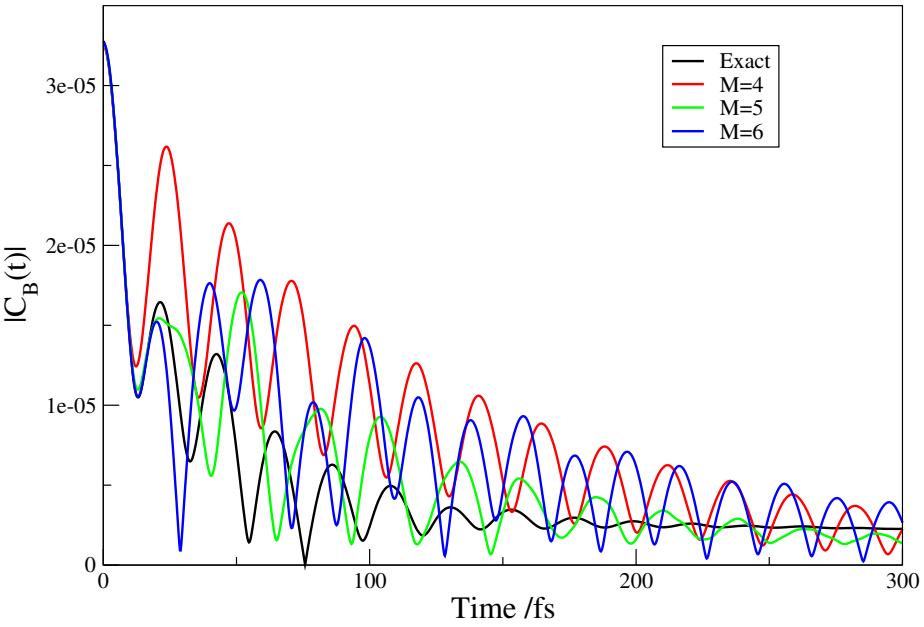

Figure 4: Bath correlation functions evaluated from Eq. (20) for $M = 4-6$ effective modes. Also illustrated is the 'exact' form $C_{\mathcal{B}}(t)$ evaluated using $J_0(\omega)$.

Fig. 5 the exciton population and coherence decay obtained from the HEOM is illustrated at various temperatures. Apart from differences in the amplitude of the periodicity of the population/coherence dynamics the population/coherence decay is temperature independent. This observation is supported experimentally by Asbury *et al.* [7, 8, 4].

Also shown for comparison in Fig. 5 is the population and coherence dynamics obtained from MCTDH wavepacket calculations. The MCTDH calculations used a discretized frequency sampling of $J_0(\omega)$ (see Ref. [6] for details) where apart from the discretization of the bath – which dictates the Poincar´e recurrence time – the calculations are taken as numerically exact at $T = 0$ K. As in Ref. [6], 60 explicit bath modes were used in the calculations, and the Poincar´e time was $T_P = 676$ fs. Over 25 fs the dynamics in Fig. 5 computed from MCTDH and the HEOM approach are very similar and the population/coherence decay to roughly the same values. Beyond 25 fs, the MCTDH dynamics appears more irregular and more strongly damped, which may be a consequence of the numerically exact treatment. However, the agreement is very good overall, in clear contrast to an $M < 5$ approximation within the HEOM scheme.

6. Summary and Conclusion

The quantum dynamics of the ultrafast exciton dissociation at the oligothiophene-fullerene heterojunction was studied, following up on earlier work of Refs. [5, 6]. The electronic part of the system was treated as an open quantum system interacting with a phonon bath. The interaction is described by a highly structured spectral density that is strongly coupled to the electronic sub-system. Such a spectral density leads to a clearly non-

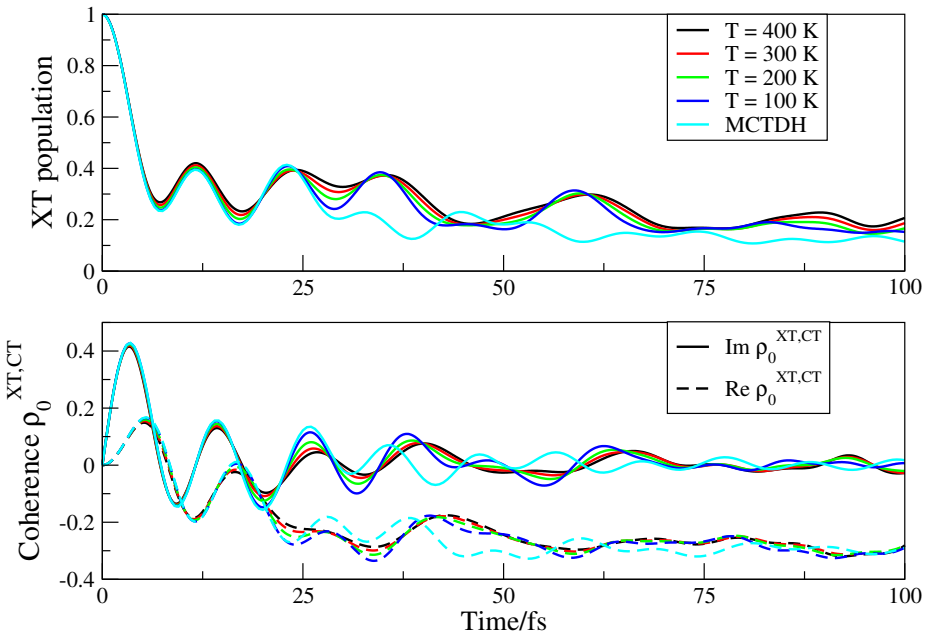

Figure 5: Dynamics of a) Exciton population and b) coherence, at various temperatures.

Markovian dynamics for the exciton dissociation. In order to compute the non-Markovian dynamics of the exciton dissociation the spectral density was reconstructed in an effective mode representation, as described in Sec. 3, using five effective modes with Ohmic closure. The bath correlation function evaluated from the effective mode spectral density which consists of a summation of exponential terms, was then used to simulate the quantum dynamics using the HEOM approach as described in Sec. 4. In view of the comparatively strong system-bath coupling in the present system, the HEOM hierarchy had to be taken to the n =10th level. Thus, the second-order TL and TNL approach that we developed earlier [36] cannot be expected to work well.

In a recent publication [53] addressing the same molecular system, an approach was used by which the first effective mode was included explicitly in the system Hamiltonian, while the residual bath was treated at second-order perturbation theory. It was found that the approach favored small diabatic couplings that arise at OT_4:C_{60} inter-fragment distance $R \geq 3.5$ ° A. The second order treatment of the residual bath cannot be expected to work well in the $R = 3.0$ ° A case considered here.

The key outcome of this work supports the experimental observation of Asbury *et al.* [7, 8, 4] that the primary charge transfer step at a typical polymer-fullerene interface is temperature independent. This confirms the analysis of Ref. [5] where wavepacket simulations were carried out in conjunction with Monte Carlo sampling over a thermal distribution.

However, one should emphasize that conclusions from the present work are limited since our study is restricted to the primary charge separation step. The ensuing generation of charge separated states and eventually free carriers, requires overcoming the electron-

hole Coulomb attraction and may necessitate thermal activation [19, 52, 2]. As shown in Ref. [12], though, the effective Coulomb barrier could be significantly lowered due to charge delocalisation, facilitating an ultrafast charge separation. A future goal is therefore to connect the present study to the sequence of follow-up processes, to complement the wavepacket simulations of Ref. [12]. A key issue will concern the initial excess energy that influences the charge separation processes and contributes to ultrafast charge separation even in systems like P3HT:PCBM that exhibit low band offsets.

Acknowledgments

Support by the joint DFG/ANR project MolNanoMat (BU 1032/3) is gratefully acknowledged.

References

[1] I. W. Hwang, C. Soci, D. Moses, Z. Zhu, D. Waller, R. Gaudiana, C. J. Brabec, A. J. Heeger, Adv. Mater. **19** (2007) 2307.

[2] C. Deibel, T. Strobel, and V. Dyakonov, Adv. Mater. **22** (2010) 4097.

[3] P. Peumans, S. Uchida, and S. Forrest, Nature **425** (2003) 158.

[4] R. D. Pensack, and J. B. Asbury, J. Phys. Chem. Lett. **1** (2010) 2255.

[5] H. Tamura, I. Burghardt, and M. Tsukada, J. Phys. Chem. C **115** (2011) 10205.

[6] H. Tamura, R. Martinazzo, M. Ruckenbauer, and I. Burghardt, J. Chem. Phys. **137** (2012) 22A540.

[7] R. D. Pensack, and J. B. Asbury, J. Am. Chem. Soc. **131** (2009) 15986.

[8] R. D. Pensack, K. M. Banyas, and J. B. Asbury, J. Phys. Chem. B **114** (2010) 12242.

[9] Z. Li, G. Lakhwani, N. C. Greenham, and C. R. McNeill, J. Appl. Phys. **114** (2013) 034502.

[10] Y. Kanai and J. C. Grossman, Nano Lett. **7** (2007) 1969.

[11] Y. Kim, S. Cook, S. M. Tuladhar, S. A. Choulis, J. Nelson, J. R. Durrant, D. D. C. Bradley, M. Giles, I. McCulloch, C.-S. Ha, and M. Ree, Nat. Mat. **5** (2006) 197.

[12] H. Tamura, and I. Burghardt, J. Am. Chem. Soc. **135** (2013) 16364.

[13] S. Gélinas, A. Rao, A. Kumar, S. L. Smith, A. W. Chin, J. Clark, T. S. van der Poll, G. C. Bazan, and R. H. Friend, Science **31** (2014) 512.

[14] H.-D. Meyer, U. Manthe, and L. S. Cederbaum, Chem. Phys. Lett. **165** (1990) 73.

[15] U. Manthe, H.-D. Meyer, and L. S. Cederbaum, J. Chem. Phys. **97** (1992) 3199.

[16] M. H. Beck, A. Jäckle, G. A. Worth, and H.-D. Meyer, Phys. Rep. **324** (2000) 1.

[17] G. A. Worth, M. H. Beck, A. Jäckle, and H.-D. Meyer, The MCTDH Package, Version 9 (2007). See http://www.pci.uni-heidelberg.de/cms/mctdh.html.

[18] J. Lee, K. Vandewal, S. R. Yost, M. E. Bahlke, L. Goris, M. A. Baldo, J. V. Manca, and T. V. Voorhis, J. Am. Chem. Soc. **132** (2010) 11878.

[19] H. van Eersel, R. A. J. Janssen, and M. Kemerink, Adv. Funct. Mater. **22** (2012) 2700.

[20] Y. Tanimura, and R. K. Kubo, J. Phys. Soc. Jpn. **58** (1989) 101.

[21] Y. Tanimura, J. Phys. Soc. Jpn. **75** (2006) 082001.

[22] A. Ishzaki, and Y. Tanimura, J. Phys. Soc. Jpn. **74** (2005) 3131.

[23] Y. Yan, F. Yang, Y. Liu, and J. Shao Chem. Phys. Lett. **395** (2004) 216.

[24] G. R. Fleming, and M. Cho, Annu. Rev. Phys. Chem. **47** (1996) 109.

[25] S. F. Huelga and M. B. Plenio, Contemp. Phys. **54** (2013) 181.

[26] K. H. Hughes, C. D. Christ, and I. Burghardt, J. Chem. Phys. **131** (2009) 024109.

[27] K. H. Hughes, C. D. Christ, and I. Burghardt, J. Chem. Phys. **131** (2009) 124108.

[28] R. Martinazzo, K. H. Hughes, F. Martelli, and I. Burghardt, Chem. Phys. **377** (2010) 21.

[29] R. Martinazzo, B. Vacchini, K. H. Hughes, and I. Burghardt, J. Chem. Phys. **134** (2011) 011101.

[30] R. Martinazzo, K. H. Hughes, and I. Burghardt, Phys. Rev. E **84** (2011) 030102.

[31] H. Tamura, E. R. Bittner, and I. Burghardt, J. Chem. Phys. **126**, 021103 (2007).

[32] H. Tamura, E. R. Bittner, and I. Burghardt, J. Chem. Phys. **127**, 034706 (2007).

[33] E. Gindensperger, H. Köppel, and L. S. Cederbaum, J. Chem. Phys. **126**, 034106 (2007).

[34] L. S. Cederbaum, E. Gindensperger, and I. Burghardt, Phys. Rev. Lett., **94**, 113003 (2005).

[35] R. Martinazzo, K. H. Hughes, and I. Burghardt, Prog. Theor. Chem. Phys. **22**, 269 (2012).

[36] I. Burghardt, R. Martinazzo, and K. H. Hughes, J. Chem. Phys. **137** (2012) 144107.

[37] U. Weiss, *Quantum Dissipative Systems*, World Scientific, Singapore, 1999.

[38] S. Mukamel, Principles of Nonlinear Optical Spectroscopy, Oxford University Press, New York/Oxford, 1995.

[39] A. Garg, J. N. Onuchic, and V. Ambegaokar, J. Chem. Phys., **83** (1985) 4491.

[40] V. May and O. Kühn Charge and Energy Transfer Dynamics in Molecular Systems, 3rd Ed., Wiley-VCH Publishers, Weinheim (2011).

[41] J. Shao J. Chem. Phys. **120** (2004) 5053.

[42] L. Chen, and Q. Shi, J. Chem. Phys. **130** (2009) 134505.

[43] Q. Shi, L. Zhu, and L. Chen, J. Chem. Phys. **135** (2011) 044505.

[44] Q. Shi, L. Chen, G. Nan, R. Xu, and Y.-J. Yan, J. Chem. Phys. **130** (2009) 164518.

[45] M. Tanaka, and Y. Tanimura, J. Phys. Soc. Jpn. **78** (2009) 073802.

[46] M. Tanaka, and Y. Tanimura, J. Chem. Phys. **132** (2010) 214502.

[47] Y. Tanimura, J. Chem. Phys. **137** (2012) 22A550.

[48] A. Ishizaki, and G. R. Fleming, J. Chem. Phys. **130** (2009) 234111.

[49] J. Strümper, and K. Schulten, J. Chem. Phys. **137** (2012) 065101.

[50] J. Zhu, S. Kais, A. Aspuru-Guzik, S. Rodrigues, and B. Brock, J. Chem. Phys. **137** (2012) 074112.

[51] Y.-A. Yan, and O. Kühn, New J. Phys. **14** (2012) 105004.

[52] C. L. Braun, J. Chem. Phys. **80** (1984) 4157.

[53] A. Chenel, E. Mangaud, I. Burghardt, C. Meier and M. Desouter-Lecomte, J. Chem. Phys. **140** (2014) 044104.

Figure 1

Click here to download high resolution image

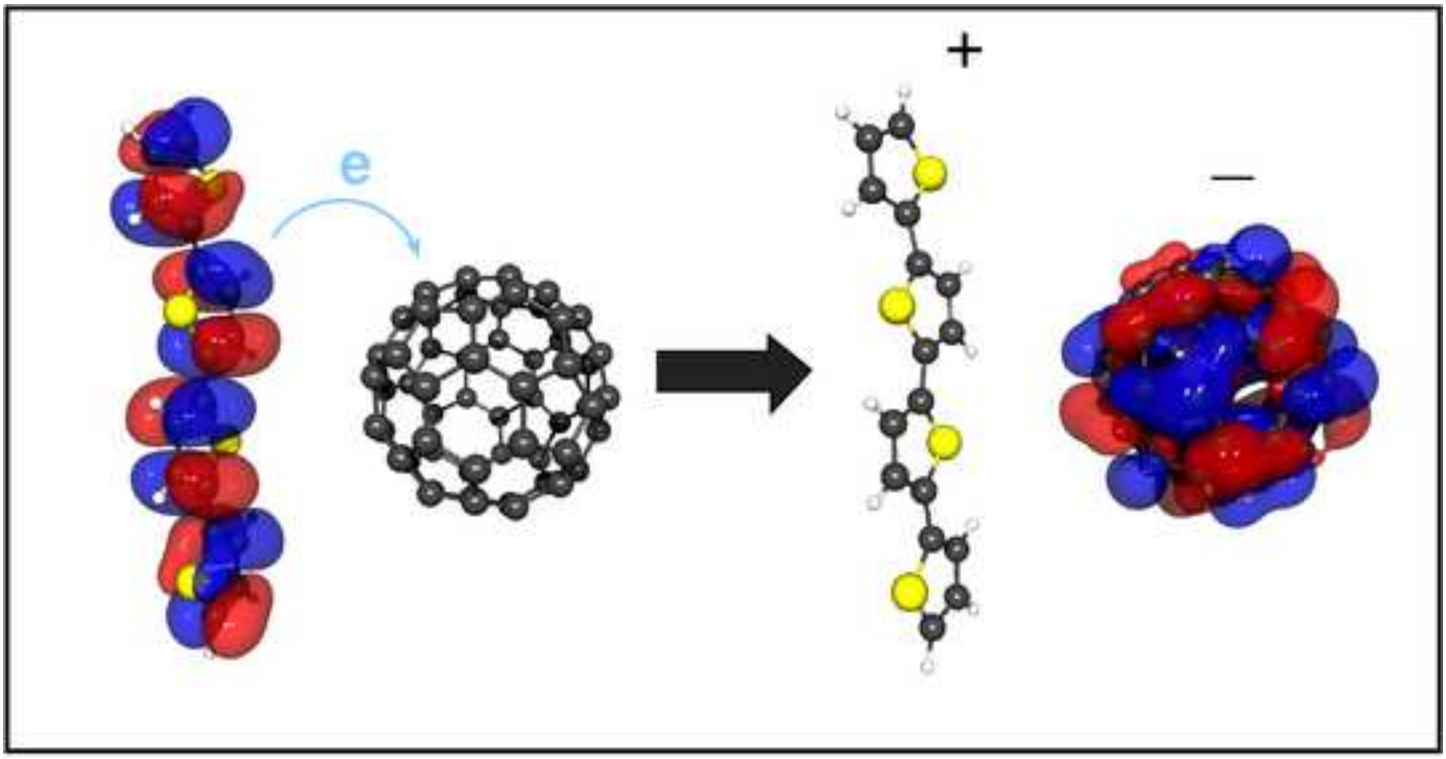

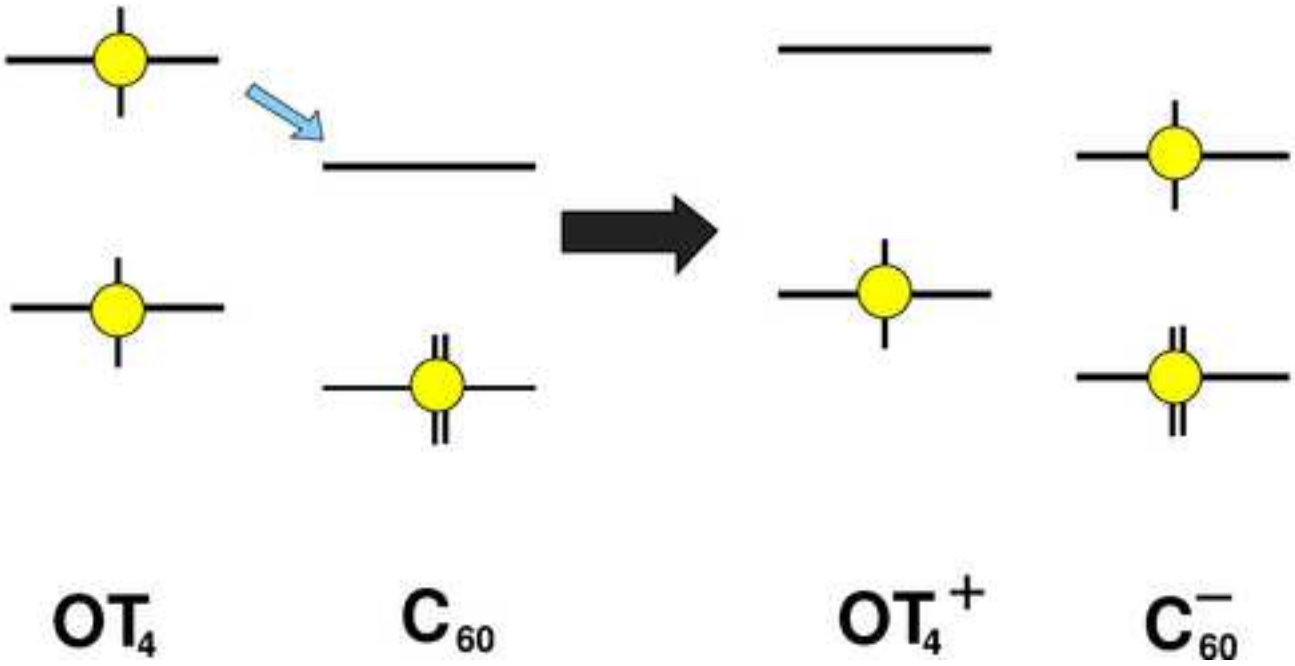

Figure 2.

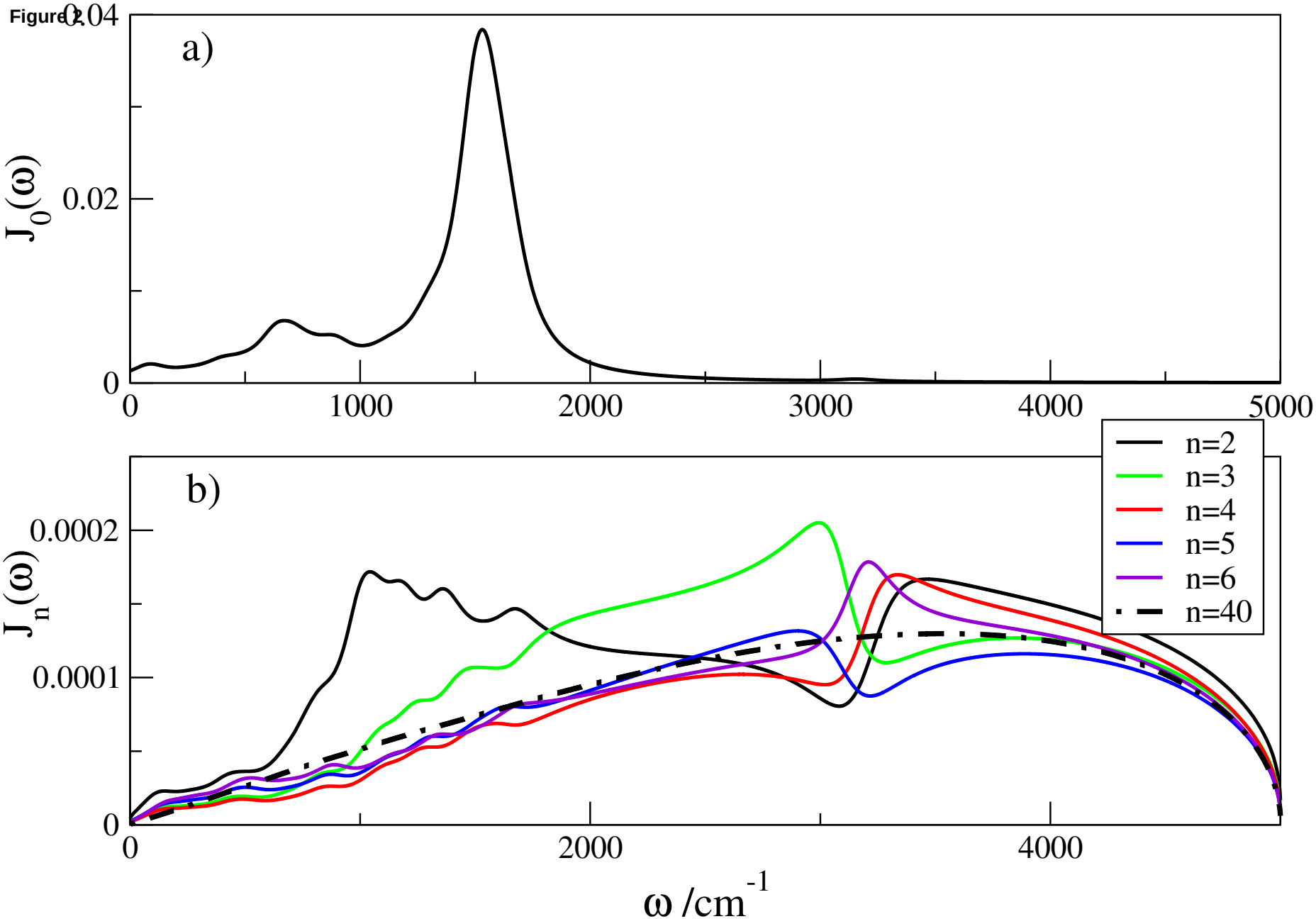
a)
b)
$J_0(\omega)$
$J_n(\omega)$
0.04
0.02
0
0
1000
2000
3000
4000
5000
0.0002
0.0001
0
2000
4000
ω /cm^{-1}
n=2
n=3
n=4
n=5
n=6
n=40

Figure 3

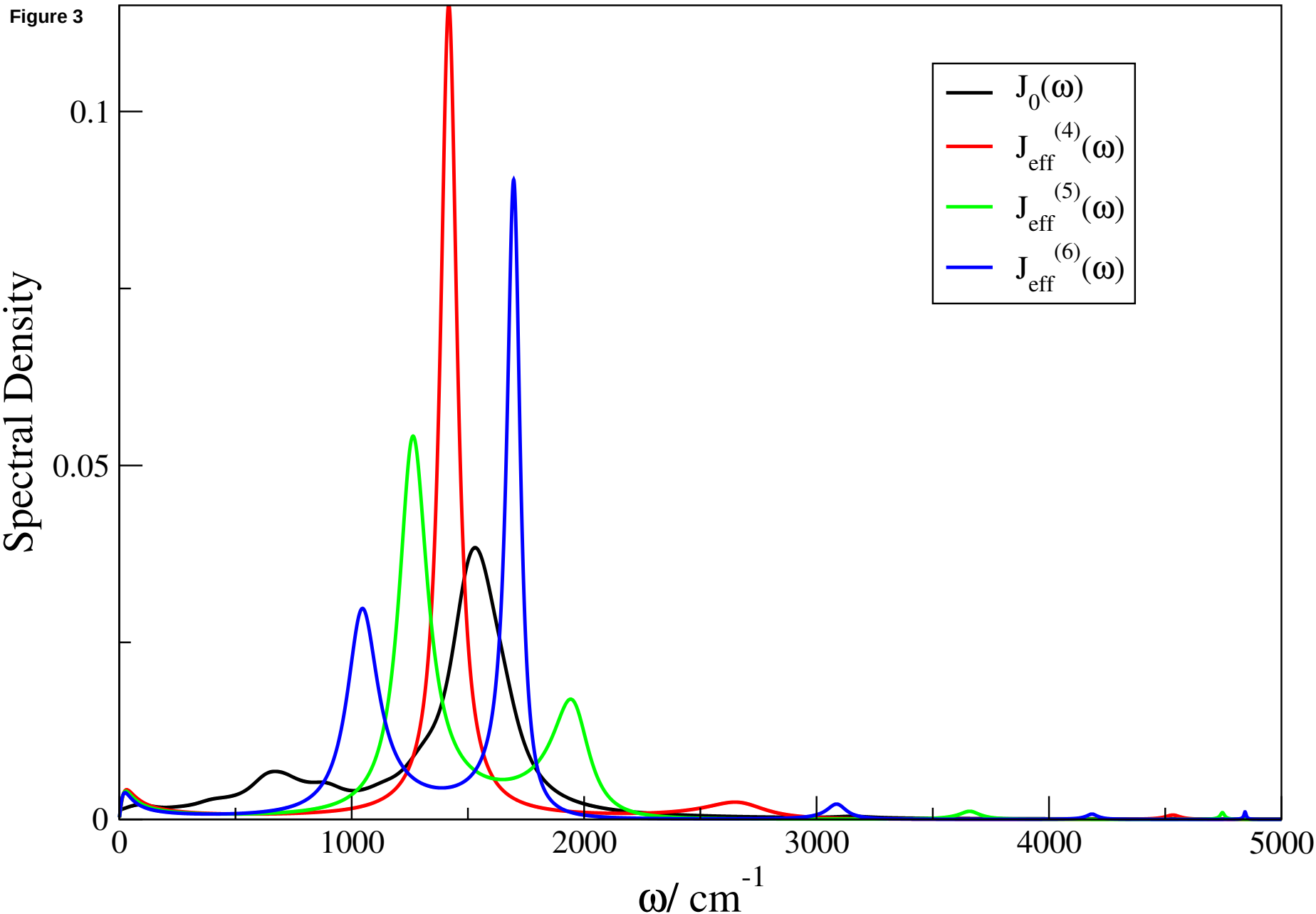
Spectral Density
0.1
0.05
0
0
1000
2000
3000
4000
5000
ω/ cm-1
J0(ω)
Jeff(4)(ω)
Jeff(5)(ω)
Jeff(6)(ω)

Figure 4

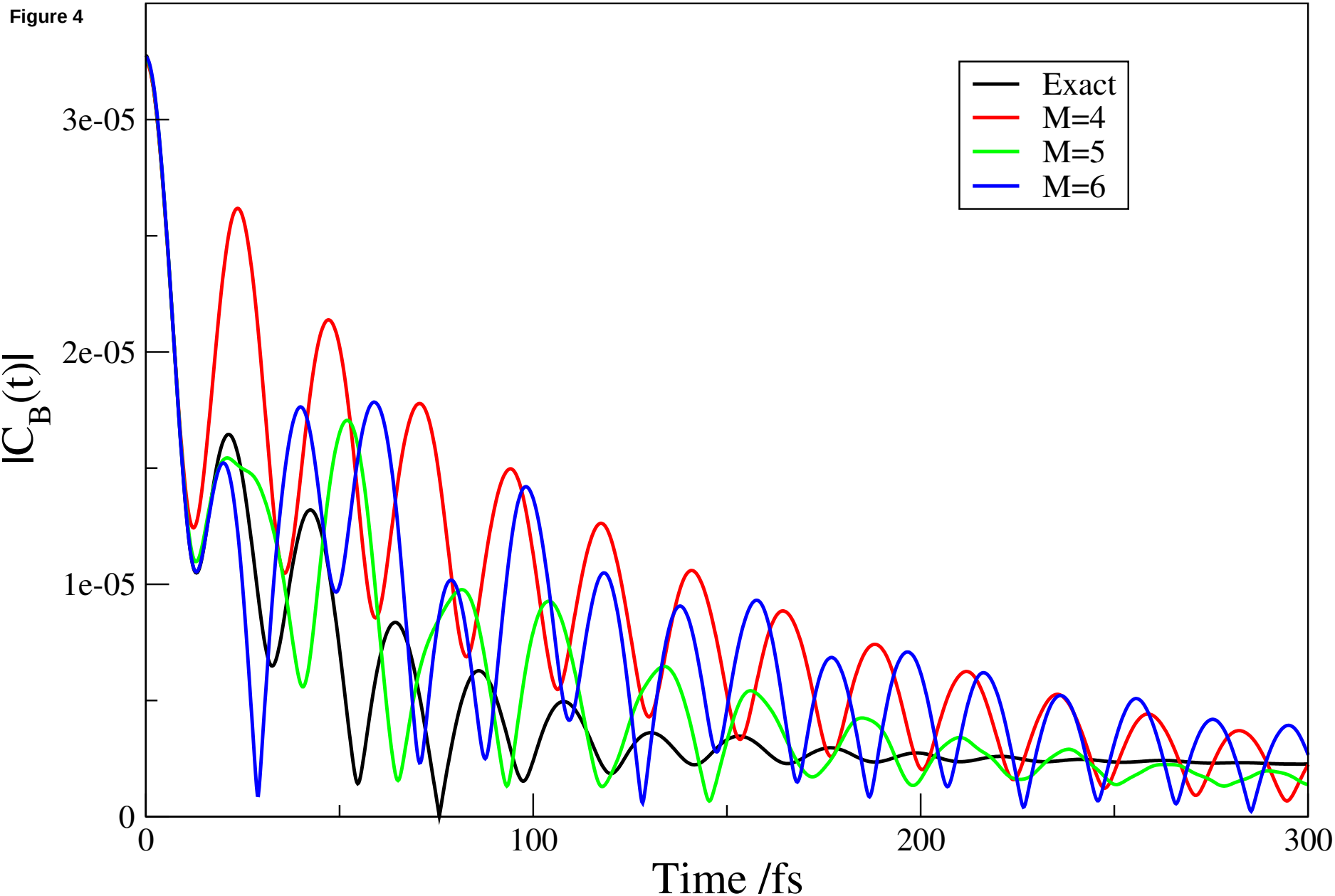

Figure 5

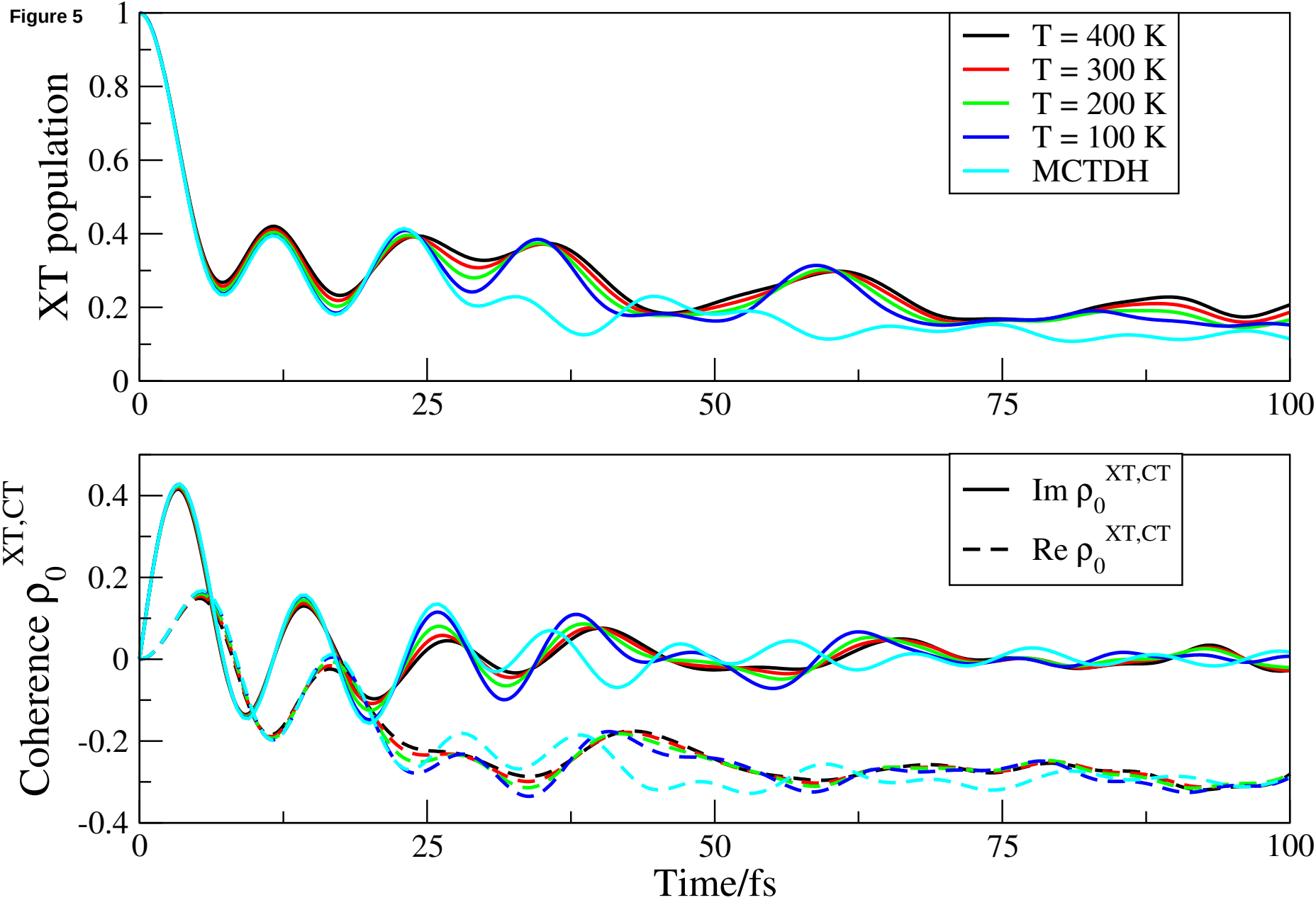
XT population
T = 400 K
T = 300 K
T = 200 K
T = 100 K
MCTDH
Coherence $\rho_0^{XT,CT}$
Im $\rho_0^{XT,CT}$
Re $\rho_0^{XT,CT}$
Time/fs

LaTeX Source Files

Click here to download LaTeX Source Files: HeteroDMCP-revRM_IB.tex